Supplementary Methods

I. Chemicals and materials.

Inorganic salts: LiCl (ultra dry, 99.9%, metal basis, Alfa Aesar), LiBr (99+%, anhydrous, Strem), LiI (ultra-dry, 99.999%, metal basis, Alfa Aesar), NaCl (puratronic, 99.999%, metal basis, Alfa Aesar), KCl (99.999%, trace metal basis, Aldrich), KBr (FTIR grade, Alfa Aesar), KI (ultra dry, 99.998%, Alfa Aesar), CsBr (99.999%, metal basis, Alfa Aesar), $ZnCl_2$ (anhydrous powder, 99.995+%, metal basis, Aldrich), $AlCl_3$ (99.99%, trace metal basis, Aldrich), $AlBr_3$ (extra pure, 98+%, anhydrous, ACROS), NaSCN ($\geq$99.99%, trace metal basis, Aldrich), KSCN (ACS reagent, $\geq$99.0%, Aldrich), $LiNO_3$ (anhydrous, 99%, Alfa Aesar), $NaNO_3$ (ACS, 99% min, Alfa Aesar), $NaNO_2$ (99.999%, metal basis, Alfa Aesar), KNO_3 (ReagentPlus, $\geq$99.0%, Aldrich), $CsNO_3$ (99.8%, metal basis, Alfa Aesar), $Ca(NO_3)_2 \cdot 4H_2O$ ($\geq$99.0%, Aldrich). $AlCl_3$ was purified by sublimation in a N_2-filled glove box (sub-1 ppm O_2 and H_2O) prior to use. NaSCN and KSCN were dried under vacuum according to reported protocols[1]. Anhydrous $Ca(NO_3)_2$ was obtained by the dehydration of $Ca(NO_3)_2 \cdot 4H_2O$[2]. Other nitrates and $NaNO_2$ were dried in a vacuum oven at about 150 °C prior to use[2,3]. The eutectic nitrate or nitrate/nitrite salts can also be prepared in the way described by Cordaro et al.[4]. *Cautious*: Most of the salts used in this work are highly hygroscopic and should be kept and handled in a N_2-filled glovebox. Molten inorganic salts with various compositions (Extended Data Table 1) were prepared by hand-grinding, followed by heating at temperatures slightly above the melting points of the molten mixtures.

Ionic liquids (ILs): 1-butyl-3-methylimidazolium chloride ($[BMIM]^+Cl^-$, 98%), 1-butyl-3-methylimidazolium tetrafluoroborate ($[BMIM]^+BF_4^-$, 98%), 1-ethyl-3-methylimidazolium ethylsulfate ($[EMIM]^+[EtSO_4]^-$, 98%), 1-butyl-3-methylimidazolium octylsulfate ($[BMIM]^+[OctSO_4]^-$, 98%), trihexyl(tetradecyl)phosphonium bis(2,4,4-trimethylpentyl)phosphinate (P^+P^-, min. 95%) were purchased from Strem. 1-butyl-3-methyl iodide ($[BMIM]^+I^-$, 99%) was purchased from Aldrich. All ILs were stored under an inert atmosphere and baked at 80 °C under vacuum for 24 h prior to use.

Metal alloys: Gallium–Indium eutectic (Ga–In, $Ga_{0.755}In_{0.245}$ (weight ratio), melting point ~ 15 °C, 99.99%, trace metal basis, Aldrich), Wood's alloy ($Bi_{0.5}Pb_{0.267}Sn_{0.133}Cd_{0.1}$ (weight ratio), melting point ~ 70 °C, stick, Aldrich) were used as received.

Organic solvents and organic ligands: Tri-*n*-octylphosphine oxide (TOPO, 99%), oleic acid (OA, 90%), oleylamine (OLA, 70%), N,N-dimethylformamide (DMF, anhydrous, 99.8%), toluene (anhydrous, ≥99.8%), acetonitrile (anhydrous, ≥99.8%), acetone (≥99.5%), methanol (anhydrous, 99.8%), ethanol (anhydrous, 200 proof, ≥99.5%), diethyl ether (anhydrous, ≥99.0%), tetrahydrofuran (THF, anhydrous, ≥99.9%), hexane (anhydrous, 95%), octane (anhydrous, ≥99%), decane (anhydrous, ≥99%), heptadecane (99%), dichloromethane (CH_2Cl_2, ≥99.9%) were purchased from Sigma Aldrich. Tri-*n*-octylphosphine (TOP, 97%) and N-methylformamide (NMF, 99%) were purchased from Alfa Aesar. OA, OLA, heptadecane, and NMF were dried prior to use in the glovebox.

II. Syntheses of nanocrystals capped by coordinating organic ligands.

Nanocrystal (NC) syntheses were performed according to reported protocols using conventional air-free techniques including Schlenk line and N_2-filled glovebox. Pt NCs (mean size about 5.5 nm)[5], Pd NCs (4.0 nm)[6], FePt NCs (3.5 nm)[7], Fe_3O_4 NCs (about 20 nm)[8], InP NCs (3.5 nm)[9,10], CdSe NCs (wurtzite, 4 nm)[11], and alpha-$NaYF_4$:Yb,Er@CaF_2 upconverting nanoparticles (UCNPs, about 23 nm)[12] were synthesized. CdSe/CdZnS core/shell quantum dots (QDs, about 6 nm, capped with phosphonic acid or carboxylic acid ligands) were provided by QD Vision, Inc.

Supplementary Discussions

I. Continuum theory for interacting surfaces in molten salts.

In this section we introduce a phenomenological theory to explain the colloidal stability observed in suspensions of various nanocrystals in inorganic molten salts. We use this phenomenological theory to predict and rationalize the layering seen in simulations purely in terms of physical interactions ubiquitous in both inorganic molten salts and organic room temperature ionic liquids: short-range steric (present in all liquids[13]) and long-range electrostatic (Coulomb) interactions between ions. Such a phenomenological theory has been used successfully to describe experimentally observed capacitive transitions at electrode-room temperature ionic liquid interfaces[14,15]. But to our knowledge, this is the first instance of its application to colloidal interactions in inorganic molten salts.

In the traditional Derjaguin–Landau–Verwey–Overbeek (DLVO) theory of interactions between colloidal particles, double-layer or electrostatic forces lead to a repulsion between charged surfaces in a solution[16]. Due to the high density of ions in a molten salt, the electrostatic forces between charged surfaces are expected to be screened out over very short distances [15]. The colloidal particles are therefore expected to aggregate because of attractive van der Waals or solute-mediated interactions. Fluctuation mediated critical Casimir-like forces between surfaces are also usually attractive (and strongly sensitive to temperature)[17].

Here we show that colloidal stabilization in molten salts can be explained by interactions not accounted within DLVO theory. We consider a scenario where surface-induced ordering or layering in the molten salt[18,19] contributes to the colloidal stability, as observed both in experiments and simulations. Such layering is expected to be pronounced and extend a long distance into the bulk if the salt is reasonably close to its crystallization temperature. In addition to surface-induced layering, interionic correlations can extend the effective screening length in highly concentrated electrolytes,[20-22] which may also contribute to colloidal stabilization in molten inorganic salts. In the following, we present our calculation for the free energy of interaction between two planar, infinite surfaces in an inorganic molten salt from a continuum Ginzburg-Landau theory perspective, taking into account both the short-range steric and long-range electrostatic interactions[23]. We first derive the oscillatory interaction energy (per unit area) between a pair of symmetric, parallel surfaces. We then show that a relative tilt between the two surfaces can lead to a repulsive free energy profile superimposed on the oscillatory profile. Such a tilt is important to account for faceting, curvature, and also surface roughness on real nanocrystal (NC) surfaces. The effects of curvature, faceting and roughness are expected to frustrate the layering and attenuate the oscillations in free energy. But it still maintains large repulsive

barriers between two approaching NCs, as shown in our simulations. Finally, the force between two plane surfaces can be generalized to that between two finite, spherical colloidal particles by using the Derjaguin approximation. It is important to note that this theory is general for investigating the interactions between particles in a solvent composed solely of ions, including colloidal NCs in inorganic molten salts. As an example, we choose CdSe NCs in molten KCl and analyze their interactions using this theory.

1. Approximate continuum Hamiltonian for density ordering.

The layering of ions normal to a flat nanocrystal (NC) surface (yz-plane) can be described using a Ginzburg-Landau model for the free energy above the critical temperature. The bulk free energy of the system (per unit area) including the effect of long-range interactions in the solvent is[24],

$$F[\psi(x)] = \int dx \left[B\big(\nabla\psi(x)\big)^2 + b\psi^2(x) + \psi(x) \cdot \int dx' V(x-x')\psi(x') \right] \tag{1}$$

In Eq. (1), $\psi(x)$ is the local charge density of the solvent expressed as the difference in number density of cations and anions normalized by the total number density of salt ions, n_s: $\psi(x) \equiv (n_+(x) - n_-(x))/n_s$. B & b are phenomenological parameters in the theory corresponding to short-range interactions and entropy. $V(x-x') = (e^2 n_s^2/\epsilon\epsilon_0)\,|x-x'|$ is the long-range effective Coulomb interaction between ions in the solvent at positions, x and x' (the problem is effectively one-dimensional as the density profile varies in the x-direction alone for infinite surfaces in the yz-plane), where e is the unit charge (on each monovalent ion), ε_0 and ε are the permittivity of free space and the relative permittivity of the solvent medium (KCl in this case). The free energy $F[\psi(x)]$ in Eq. (1) is the effective one-dimensional Hamiltonian for describing the molten salt. We ignore the $\psi(x)^4$ and higher order terms because the molten salt (KCl) is above its bulk melting temperature and is a disordered liquid far from the colloidal interface. The effect of long-range interactions is simplified in Fourier-space. By expanding around the wave-vector, q_0, at which the free energy is minimized, the free energy of Eq. (1) can be approximated as,

$$F[\psi(x)] \simeq \frac{|b|l_c^2}{8q_0^2} \int dx \left[\big((\nabla^2 + q_0^2)\psi(x)\big)^2 + 4q_0^2 l_c^{-2}\psi^2(x) \right] \tag{2}$$

where q_0 is the preferred wavenumber of layering and l_c, the decay length of the layering, is related to the Ginzburg-Landau correlation length ($\sqrt{B/|b|}$). The preferred wavenumber of layering is given by[15], $q_0 = (1/\,l_c\,l_s\,)^{1/2}$, where l_c can be of order of several nanometers (nm), and l_s is the Debye screening length (within the Debye-Hückel theory applicable to dilute electrolytes), which is around 0.1 nm (comparable to ionic radius) in inorganic molten salts. The wavelength of ordering can then be a few

angstroms which is about one ionic layer thick as expected. The solvent can thus exhibit layering up to a long length-scale (much longer than the classical Debye screening length) as a result of the competition between steric and Coulomb interactions. Indeed, estimates of the screening length obtained by analyzing the poles of the structure factor are much larger than the Debye length (even in the Gaussian approximation used here).

Such an effective Hamiltonian has been used to describe a variety of materials whose ordering is governed by a competition between short- and long-range interactions[24] – for example, magnetic films, diblock copolymers, Langmuir monolayers, and more recently, ionic liquids[14,15,25] – and the corresponding phase diagram has been extensively studied and characterized[23,26]. This is richer than that for a simple liquid: as the temperature is lowered towards the bulk ordering temperature, the liquid can go from being disordered to an intermediate regime characterized by local structural order before long-range crystalline order is established. In Eq. (2), we consider the molten salt to be above its ordering temperature, so that while the bulk is disordered, a nanocrystal surface can template local order in its vicinity[24,27].

An Euler-Lagrange minimization of this Hamiltonian in the bulk results in a fourth-order linear differential equation that can be solved analytically,

$$\frac{d^4\psi}{dx^4} + 2q_0^2 \frac{d^2\psi}{dx^2} + q_0^2 \cdot (q_0^2 + 4l_c^{-2})\psi(x) = 0 \tag{3}$$

With the appropriate surface boundary condition (determined by the chemical interaction of the surface with ions) and charge neutrality conditions, one can solve the charge density profile, $\psi(x)$. An approximate solution for $\psi(x)$ induced by one surface that satisfies a simple boundary condition that a fixed number of anions bind to the surface, $\psi(0) = \psi_0$, and global charge neutrality, is given by

$$\psi(x) = \psi_0 \sec(\phi) e^{-x/l_c} \cos(q_0 x + \phi) \tag{4}$$

where ψ_0 is the ion density at the surface fixed by the strong surface-binding affinity. The phase, $\phi = \tan^{-1}(1/(q_0 l_c))$, ensures charge neutrality in the bulk of the solvent. This form of the charge density arises since the NC (e.g., Cd-terminated CdSe NCs) surface has a strong preference for one type of ions (i.e., Cl^-) in the melt, which in turn leads to successive alternating layers of cations and anions (with wavenumber q_0) decaying with distance from the surface (with a range of l_c).

2. Density order and free energy in two-surface geometry.

Having solved the charge density ordering near one surface, we now solve for the corresponding order between two surfaces. This can be used to calculate a free energy profile for the interaction

between two NC surfaces as a function of their distance of separation. Colloidal stability may result from large barriers (compared to k_BT) in this free energy landscape.

1) Parallel surfaces. The Euler-Lagrange differential equation, Eq. (3) corresponds to the approximate model Hamiltonian that describes the competition between short- and long-range interactions (Eq. (2)). It is analytically solvable and can be generalized easily to the case where there are two *symmetric* surfaces in parallel (located at $x = L$ and $x = -L$) that induce order as,

$$\psi_\parallel(x) = \psi_1 cos(q_0 x)cosh\left(\frac{x}{l_c}\right) + \psi_2 sin(q_0 x)sinh\left(\frac{x}{l_c}\right) \tag{5}$$

where the solution is symmetric about the mid-plane ($x = 0$) by construction and the two constants ψ_1 and ψ_2 are to be determined from two conditions: the surface boundary value and charge neutrality.
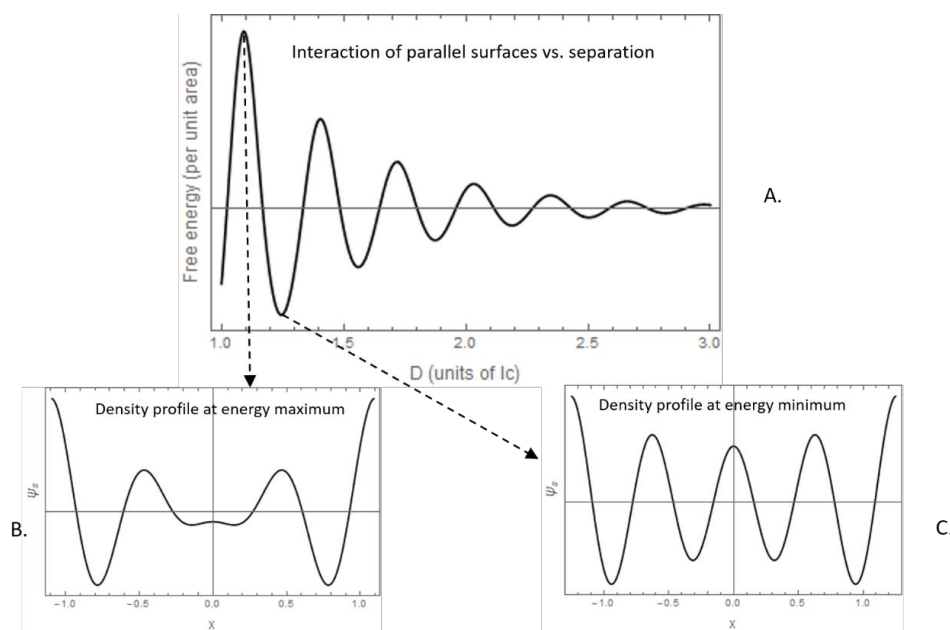

Fig. S1. Theoretical analysis of two symmetric parallel surfaces. **(A)** Free energy of interaction per unit area of two parallel plane surfaces (expressed as a ratio of the phenomenological energy scale ($F_0 \sim bl_c\psi_0^2$) as a function of the distance of separation (D) between them, expressed in units of the correlation length l_c (around 1 nm). The wavenumber of layering, $q_0 = (1/l_c l_s)^{1/2}$ is estimated to be 10 nm^{-1}, (wavelength of layering in KCl ~ 6 Å). An estimation of the energy scale for F_0 is available on Page S11 and from the simulation result (Fig. S8A). Charge density profiles, $\psi(x)$, corresponding to a free energy **(B)** maximum and **(C)** minimum. This illustrates that configurations where an integer number of layers can be fit in between two surfaces are energetically favorable.

The charge neutral symmetric solution in Eq. (5) can be reduced to the simplified, intuitive form when the separation between the surfaces, $D = 2L$, is large,

$$\psi_{\parallel}(x) = \psi_0 \left[\exp\left[-\frac{L-x}{l_c}\right] \cos(q_0(L-x) + \phi) + \exp\left[-\frac{L+x}{l_c}\right] \cos(q_0(L+x) + \phi) \right] \tag{6}$$

where the pre-factor, ψ_0, is determined from the surface boundary condition. This solution is simply interpreted as the superposition of two single-surface solutions originating from $x = L$ and $x = -L$ respectively with equal weight (since the surfaces are identical). We use this simpler expression to plot the symmetric density profile in Fig. S1, and calculate the total free energy by inserting the expression in Eq. (6) into Eq. (1),

$$F_{\parallel}(D) \simeq -\left(\frac{1}{2}\right) b l_c \psi_0^2 \cdot e^{-\frac{D}{l_c}} \cos(q_0 D + \phi) \tag{7}$$

2) Tilted surfaces.

Our simulations show that there is an exponentially decaying repulsive component over and above the oscillatory features in the free energy, particularly apparent in the 20° tilted plates (Figs. 3e &S8B). This is related to the large energy cost of removing the last few remaining ionic layers as the two NC surfaces approach very close to each other[28]. A qualitative way of understanding this repulsion in terms of the phenomenological theory is presented here.

An obvious effect of tilting one surface with respect to the other is that the separation between the two plates is different at different positions, leading to an averaging out of the oscillatory interactions to some extent. By integrating Eq. (7) over the range of separation: $D_{max} - D_{min} = l_p sin\theta$, where l_p is the size of the plate (corresponding to the size of the NC facet) and θ is the angle of tilt, one can obtain the factor by which the oscillations are attenuated: for large facet areas and/or large angles of tilt, the oscillations are averaged out to a large extent and an approximate form for the attenuation factor is $\eta \sim q_0 l_p sin\theta$, whereas for small plates tilted at small angles, i.e., in the limit $l_p sin\theta \ll l_c$, the attenuation factor scales as $\eta \sim 1 + l_p sin\theta / l_c$. We indeed see an attenuation in the free energy oscillations in the simulation results for plates tilted at larger angles (Fig. S8B). However, for NCs of small size, such as used in this experiment, and strong surface-induced layering (i.e., high energy peaks), the attenuation is not strong enough to completely wash out these oscillatory features (Fig. S8B).

When one of the order-inducing surfaces is tilted with respect to the other, the order is induced along different axes (See cartoon in Fig. S2A). This can be analyzed as an effective one-dimensional problem by considering variations of the charge density along the x-axis, assuming the two surfaces induce different effective layering wavenumbers, q_l and q_r, respectively, where $q_l = q_r cos\theta$. The

density profile can be approximately calculated by superposing the one-surface solutions from the left and the right,

$$\psi_{tilt}(x) = \psi_0\left[\exp\left[-\frac{L-x}{l_c}\right]\cos(q_r(L-x)+\phi_r) + \exp\left[-\frac{L+x}{l_c}\right]\cos(q_l(L+x)+\phi_l)\right] \qquad (8)$$

where the asymmetry between the surfaces leads to different preferred wavelength of order induced by left and right surfaces. We expect this Ansatz to be more accurate when the plate separation, $D = 2L$, is significantly larger than the correlation length, l_c.

Putting the Ansatz for density profile, Eq. (8), into Eq. (2), we calculate numerically the free energy of interaction of two surfaces as a function of their separation, $F(D)$, for different degrees of tilt as shown in Fig. S2.
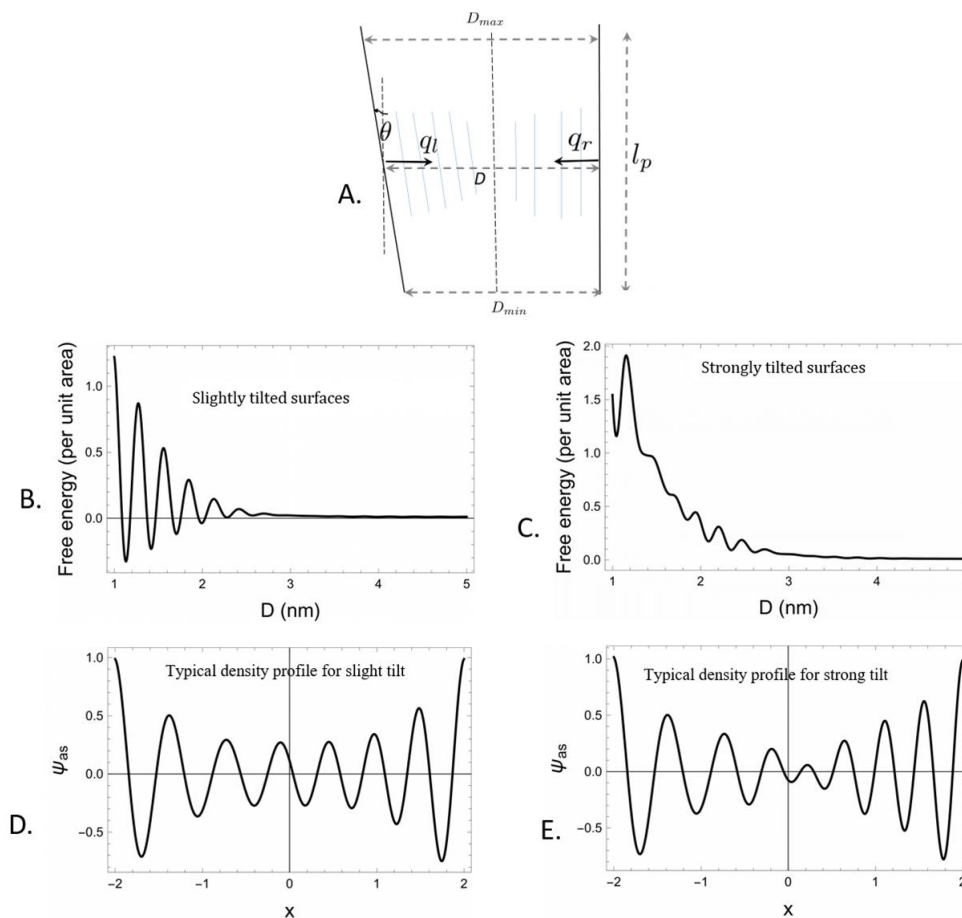

Fig. S2. Theoretical analysis of two tilted surfaces. **(A)** Layering induced by a pair of surfaces tilted relative to each other (θ) such that the order from each surface is characterized by two different wavenumbers along the x-axis, q_l and q_r, respectively. **(B,C)** The effect of the frustration in layering induced by the tilt on the oscillatory-repulsive interactions. The wavenumbers on the left and right, q_l and q_r, are **(B)** 10 and 12 nm^{-1} (slight tilt), and **(C)**. 10 and 14 nm^{-1} (stronger tilt), respectively. (A

wavenumber of 10 nm^{-1} corresponds roughly to layering in KCl.) All lengths in the plots are in terms of the correlation length, $l_c = 1$ nm, and the energy scale is $F_0 \sim bl_c\psi_0^2$, the same as in the case of parallel surfaces. The corresponding charge density profiles, $\psi(x)$, at a plate separation given by $L = 2$, for **(D)** the small angle tilted and **(E)** large angle tilted cases, respectively.

The relative tilt between the ordering from the right and left surfaces (Fig. S2A) is reminiscent of a grain boundary in a crystalline ordered phase. The creation of a grain boundary, which is a defect in the ordering, requires a positive free energy cost. The energy cost increases with the tilt angle[29] as has been shown in the context of defects in lamellar ordering in block copolymers[30]. The two surfaces would therefore tend to move away from each other to reduce this free energy cost (which scales as square of the amplitude of order parameter), therefore resulting in an effective repulsion. We expect this repulsive free energy cost to scale as, $F_{tilt}(D,\theta) \sim F_0 e^{-\frac{D}{l_c}}(l_c q_0)^{-1}\theta^2$.

To summarize, the interaction between two parallel flat surfaces is a decaying and oscillatory function of their distance of separation (D), being minimized at the special separations where commensurate layering can occur, i.e., an integer number of ionic layers can fit in between the two plates. On top of this, there are repulsive interactions between two tilted plates which is an effective function of the angle of tilt (θ). The total free energy of interaction between two mutually tilted flat surfaces, for a small angle of tilt, can then be captured by the following semi-empirical expression where the effect of the tilt is taken into account

$$F(D,\theta) = F_{\parallel}(D) + F_{tilt}(D,\theta) \sim F_0 e^{-D/l_c}(\cos(q_0 D) + f(\theta)), \tag{9}$$

where $f(\theta) \sim (q_0 l_c)^{-1}\theta^2$ is the tilt-dependent repulsive part (square of angle of tilt for small angles since the direction of tilt is unimportant).

3) Curved surfaces.

Given the detailed results for interactions of flat surfaces (parallel or tilted) from both continuum theory and atomistic simulations, we now generalize them to spherical NCs. The approximation developed by Derjaguin is commonly used to calculate the force of interaction between curved surfaces[28], given a theoretical expression for free energy of interaction between flat surfaces. We outline this procedure in its most standard form and then adapt it to the free energy for the oscillatory tilt-dependent interactions in molten salts. The interaction between two identical spheres (of radius R)

separated by a distance D is calculated by integrating over ring-like circular surface elements of thickness dr and area $2\pi r dr$. The relevant geometry is sketched in Fig. S3A. The distance between rings at position r is given by, $z(r) = D+2R(1-\cos(\theta)) \sim D+r^2/R$. When $D < R$, the effective interaction between the spheres can then be written as,

$$V_e(D) \simeq 2\pi \int_0^\infty F(z) r dr = \pi R \int_D^\infty F(z) dz \tag{10}$$

where $F(z)$ is the interaction energy of a circular surface element with the opposite surface, assumed to be locally flat. The above analysis can be applied directly to the interaction between parallel surfaces. With necessary integrals, we get,

$$V_\parallel(D) = \pi R \int_D^\infty F_\parallel(z) dz = \frac{\pi R F_0}{\left(q_0^2+l_c^{-2}\right)^{1/2}} e^{-D/l_c} \cos(q_0 D) \tag{11}$$

which for rapidly oscillatory interactions, $q_0 \gg l_c^{-1}$, simplifies to: $V_\parallel(D) \simeq \pi R q_0^{-1} F_\parallel(D)$.

The above form of the approximation is appropriate for the typical layering/solvent structuring interactions between colloids. However, DLVO forces, electrostatic or van der Waals, depend only on the distance of separation of the surfaces and their area. To compare the layering force with the DLVO forces, we have to modify this procedure to effectively account for the tilt. We integrate over the same circular surface elements shown in Fig. S3A, bearing in mind that the average angle of tilt in each circle is θ, being related to the distance of separation as, $z(\theta) = D + 2R (1-\cos^2 \theta) D + R\theta^2$, for small angles. The total interaction energy is then found by performing the integral of F_{tilt} introduced in Eq. (9) over these surface elements as,

$$V_{tilt}(D) = 2\pi F_0 \int_0^\infty e^{-z/l_c} \theta^2 r \, dr \simeq \pi l_c^2 F_0 e^{-D/l_c} \tag{12}$$

The contribution to the free energy of interaction from the tilt, scales differently (and with a *lower power*) with R than the interaction between parallel surfaces. The physical meaning of this is apparent when we write the total effective energy of interaction between spherical surfaces by combining Eq. (11) and (12), as:

$$V_e(D) \simeq \pi R l_c F_0 e^{-D/l_c}(\cos(q_0 D) + l_c/R) \tag{13}$$

Eq. (13) shows that the oscillatory (and symmetric) interactions between parallel surfaces become more pronounced as R is increased, i.e., the surfaces approach the flat limit, while the repulsive component increases when R is small, as now the surface elements sample greater tilt angles. This R-dependence is as per our physical expectations and is illustrated in Fig. S3B. Note the free energy (in k_BT) in Fig. S3B was estimated from the free energy per unit area, F_0, as described below. We also compare the typical DLVO forces (See more details in the estimation of DLVO forces in the Appendix)

with the layering interactions for a typical spherical particle (4 nm diameter) used in experiment in Fig. S3C. The dependence of the colloidal interactions on the size of the colloidal nanoparticles suggested in Eq. (13) would be interesting to probe in subsequent experiments. Particularly, kinetic trapping by large oscillatory barriers may become increasingly relevant for larger colloidal particles where the repulsive component becomes relatively smaller.
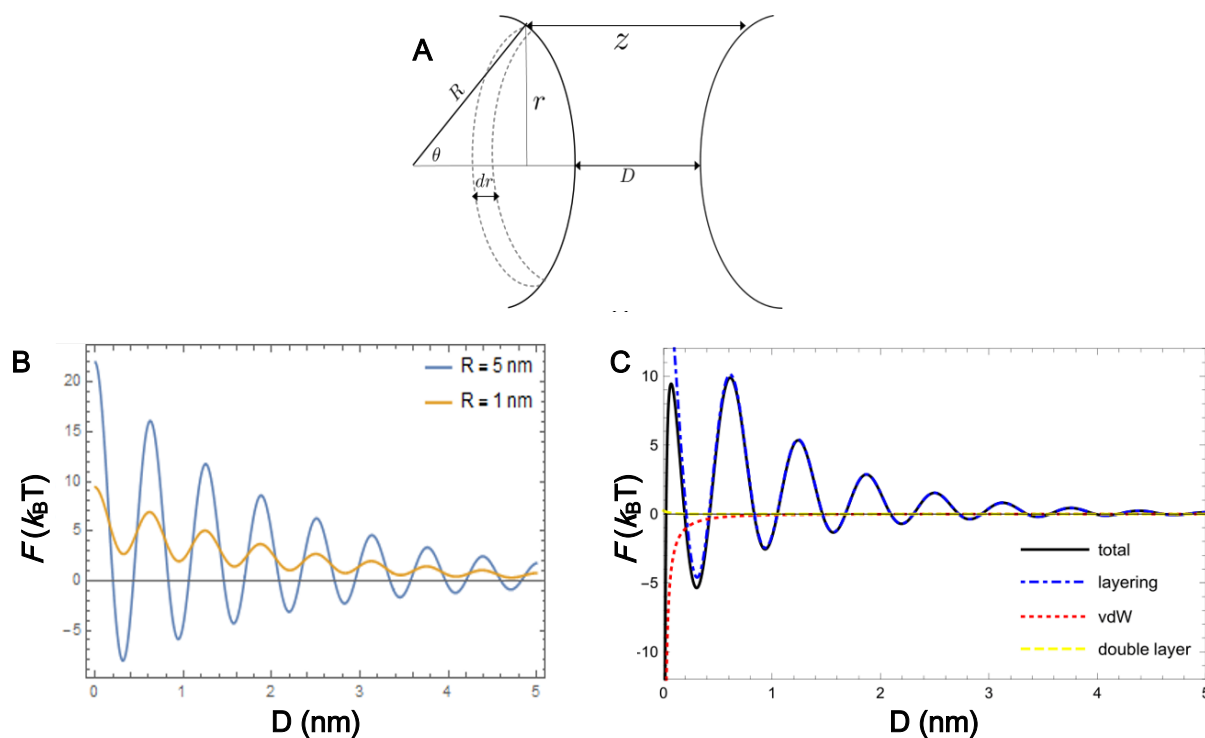

Fig. S3. Theoretical analysis of two curved surfaces. **(A)** Relevant geometry for Derjaguin approximation. **(B)** Free energy of layering as a function of the distance of separation (D) between two spherical particles, calculated from the simplified expression given in Eq. (13) for parameter values in the free energy scale, $F_0 \sim b l_c \psi_0^2$, estimated from simulation (Fig. S8A) to be about 20 k_BT/nm^2. This illustrates that the repulsive interactions become more important relative to the oscillatory interactions for smaller particle radius. **(C)** Layering/solvation interaction between spherical particles (4 nm in diameter) compared to DLVO interactions. Note that DLVO forces become significant enough compared to the layering forces only at very short sub-nm separations. This is also shown explicitly for a 10 nm diameter quasi-sphere from simulations (Fig. 3f in the Main Text).

Estimate for energy scale The free energy (per unit area) scale, $F_0 \sim b \, l_c \psi_0^2$, is in terms of phenomenological parameters that need to be determined from experiment or a more microscopic

theory. However, an estimate for the free energy scale can be made by relating the coarse-grained parameters to a picture of particles on a lattice: $b \sim k_B T / a^3$, where a is the lattice constant related to the size of the ions in molten salt ($a \sim 5$ Å). The ionic density, n_s, is related to the lattice constant, $n_s \sim 1/a^3$. Assuming $l_c \sim 1$ nm and a strong binding to the surface, $\psi_0 = 1$, we get a free energy scale of 10 k_BT/nm^2. Using this on a 2×2 nm NC surface, and the expression for interaction energy versus distance between parallel plates in Eq. (7), we estimate an interaction energy of the order of 10 k_BT at a separation of about 1 nm comparable to the energy scale seen in the simulations of flat surfaces (Fig. S8A).

II. Molecular dynamics (MD) simulations of CdSe NCs in molten KCl.

In addition to the analysis with continuum Ginzburg-Landau theory, we ran MD simulations of CdSe NCs in KCl solvent[31]. The details for MD simulations are included in the Appendix. Along the same lines as the theory discussed above, we start our MD simulations by considering ion layering around a single CdSe NC surface. Then we simulate the interactions between two parallel surfaces in molten salts, especially along the axis normal to NC surface. We generalize such interactions to two tilted surfaces and finally quasi-spherical NCs. For comparison, we also run simulations of structureless, or chemically inert, walls in molten KCl. There have been several reports on the influence of molecular layering on forces between colloids and nanoparticles using continuum theory and MD simulations in room temperature ionic liquids[32]. However, to the best of our knowledge, there has been no quantitative theoretical studies for the forces between colloids induced by an inorganic molten salt.

In general, solid surfaces are expected to induce liquid density oscillations[13,33]. In densely charged liquids, solid surfaces with surface charge are known to induce even longer range charge density oscillations[15,27]. As expected, we observed robust layering of the K$^+$ and Cl$^-$ ions near the surfaces of the nanoparticles (normal to the NC surface: Fig. S4). In addition to ion layering in the direction normal to the interface, significant in-plane ordering of K$^+$ and Cl$^-$ ions was observed near the crystal surface (Fig. S5C–F), because of a good match between the in-plane periodicity of the CdSe surface and the diameters of ions in the molten salt. The in-plane correlation functions describe the statistically-averaged, in-plane distances between particles and their neighbors. As in-plane ordering increases, the peaks will become sharper and will decay less with distance. For example, a system with no in-plane ordering will display a constant value for all separations, while a solid will have sharp peaks that extend as far as desired without decay.

We quantified the net interaction between two rectangular cuboid zinc-blende CdSe NCs (hereon referred to as "nanocubes") of dimension $2.45\times1.85\times1.85$ nm^3 in solution along the axis normal to NC surface using standard enhanced sampling techniques (specifically umbrella sampling)[34-36]. In addition, we fit the charge density profile shown in Fig. S4 with the Ginzburg-Landau theory. In detail, we extracted the length-scales, the correlation length (l_c) and the oscillation frequency (q_0) from the density profile in Fig. S4 by fitting the expression for the charge density with Eq. (4). Using l_c and q_0, we were able to find correspondence between simulation and theory using a two-parameter fit of Eq. (9) for the amplitude, F_0, and f(θ).

We focused on interactions between Cd-terminated CdSe [001] facets, but also collected data for the interaction of a [001] Cd-terminated facet interacting with a [111] Cd-terminated facet; the nanocube interactions were indistinguishable (Fig. S6). We conclude that the main effect here is solvent layering along the surface normal, and that in-plane ordering effects due to surface atom arrangement is less important. For simplicity, we fixed the orientation of the nanocubes, and only allowed motion along one axis, which is normal to the NC surface.
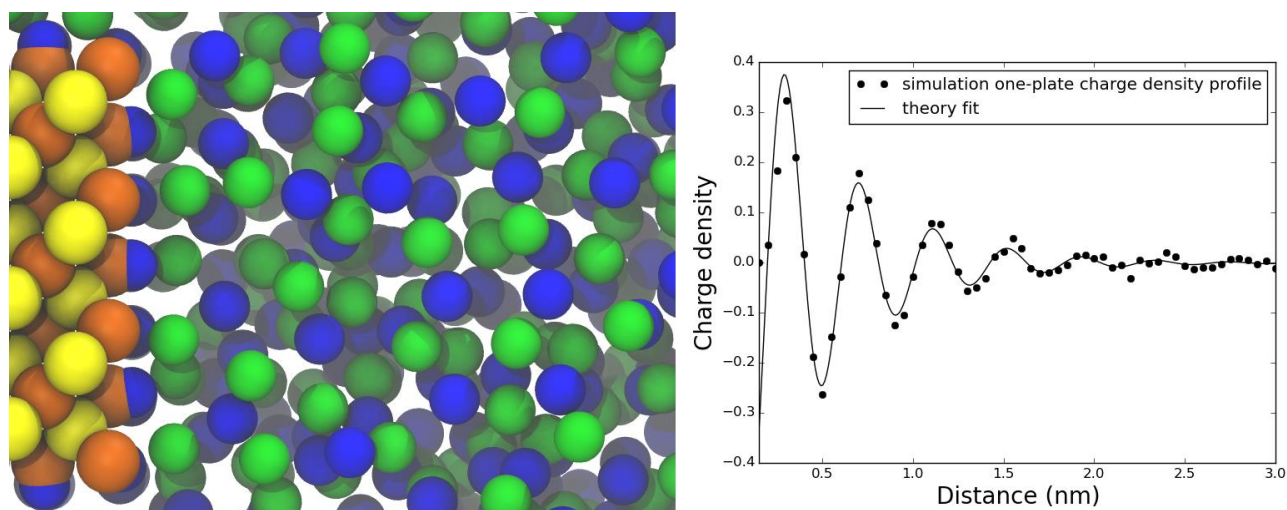

Fig. S4. The chemical affinity between Cd-terminated [001] CdSe surface and Cl$^-$ induces charge density oscillations in molten KCl. (Left) A snapshot of layering of ions around the [001] surface of a CdSe nanocube ($2.45\times1.85\times1.85$ nm^3); **(Right)** The simulated charge density as a function of the distance away from CdSe surface (black dots) and the fit with Ginzburg-Landau theory (solid line); note the first Cd-bound Cl$^-$ peak has been omitted from the charge density profile. Color code in the snapshot: Orange: Cd, yellow: Se, green: K$^+$, and blue: Cl$^-$.
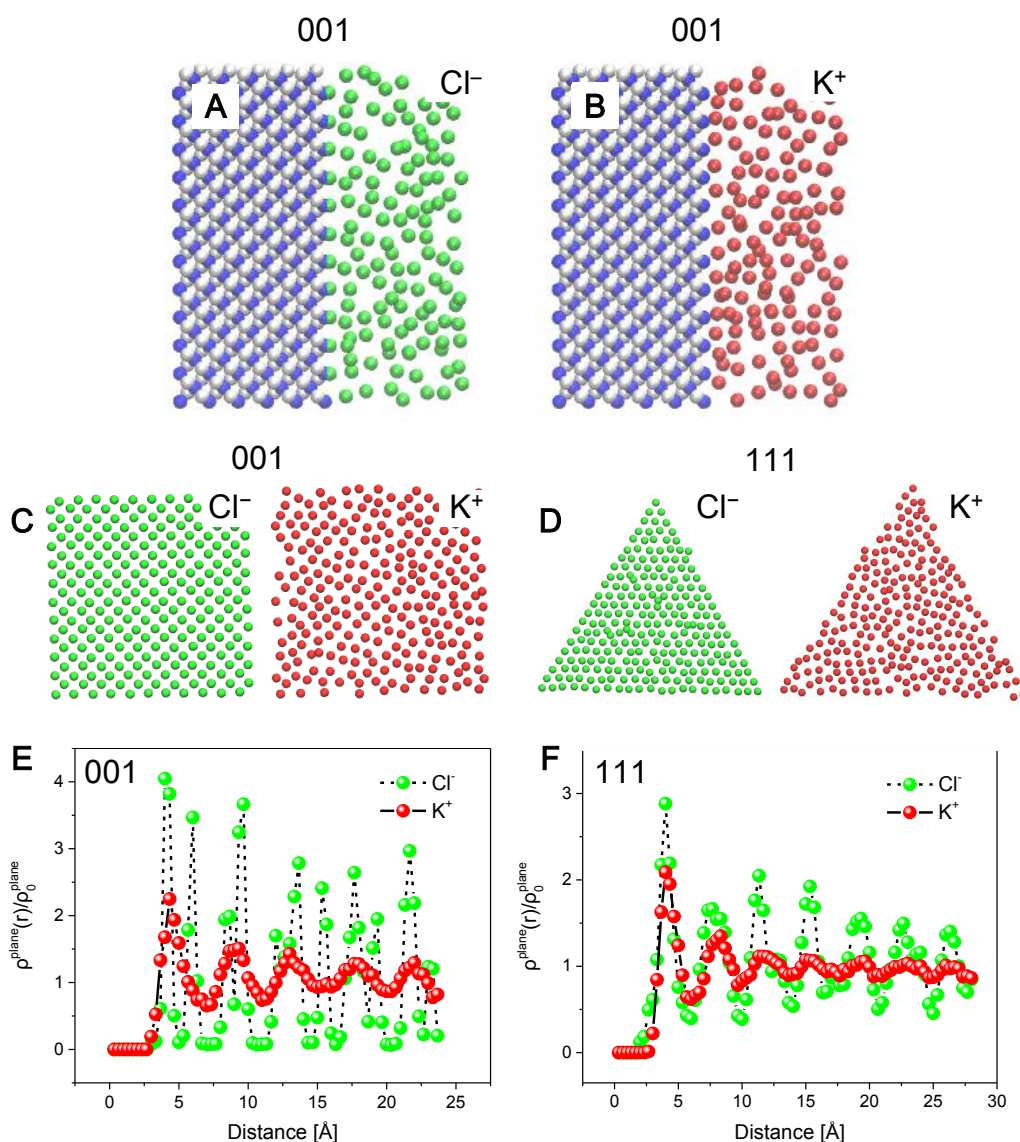
Fig. S5. MD simulations of CdSe crystal in molten KCl. Snapshots of MD simulations showing the distributions of **(A)** Cl$^-$ and **(B)** K$^+$ ions near [001] surface of zinc-blende CdSe crystal. **(C,D)** Snapshots of MD simulations and **(E,F)** in-plane density profiles showing significant in-plane ordering in the first layer of Cl$^-$ and K$^+$ ions near **(C,E)** the [001] surface and **(D,F)** the Cd-terminated [111] surface of the zinc-blende CdSe crystal. Color code for the snapshots in (A–D): Blue: Cd; white: Se, green: Cl$^-$, red: K$^+$.
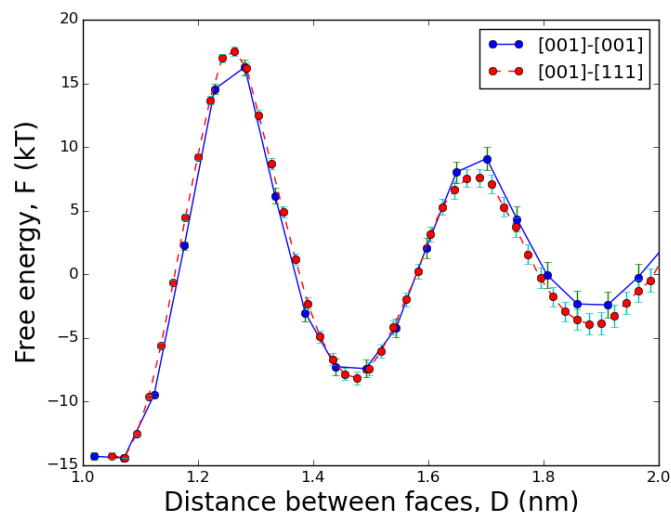
Fig. S6. Simulated free energies of layering between two surfaces of CdSe nanocubes, [001]-[001] (blue) and [001]-[111] (red), in molten KCl. The indistinguishable free energies of interactions between different facets indicate the ion layering is the dominant factor.
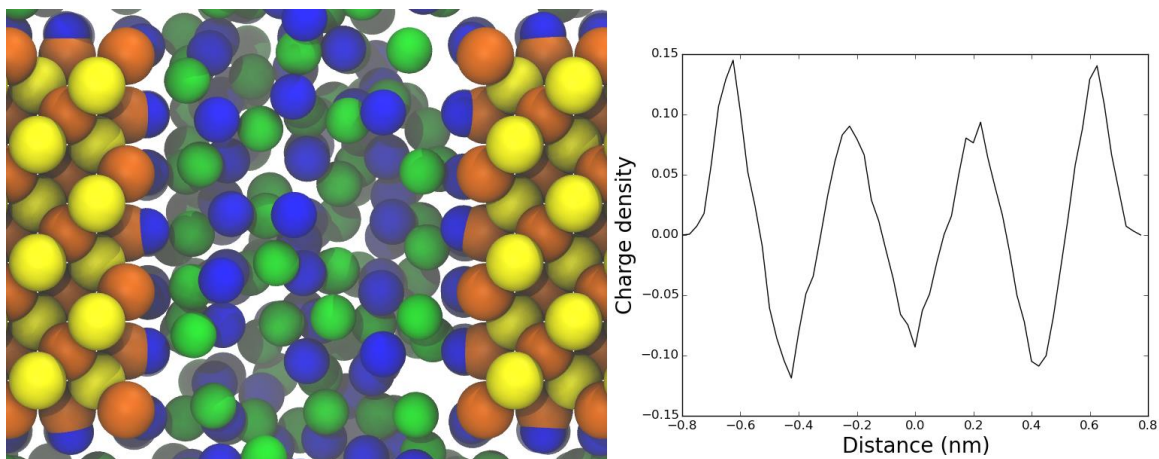

Fig. S7. An example of parallel CdSe nanocubes in molten KCl and the corresponding charge density profile. (Left) A snapshot of layering of ions between two [001] surfaces of CdSe nanocubes ($2.45 \times 1.85 \times 1.85$ nm^3); **(Right)** Simulated charge density as a function of the distance between two surfaces; note the Cd-bound Cl$^-$ peaks have been omitted from the charge density profile. Color code in the snapshot: Orange: Cd, yellow: Se, green: K$^+$, and blue: Cl$^-$. Here, the density profiles templated by the nanocubes constructively interfere, and so this configuration is at a free energy trough. Note that the bound layer of Cl$^-$ ions are not shown in the charge density profile.

Parallel nanocubes induced charge density oscillations in the KCl solvent which interfered at the midplane when the nanocubes came close together (Fig. S7). The interference leads to a decaying, oscillatory energy of interaction between nanocubes as a function of separation, D (Fig. S8A). If we envision two nanocubes coming together along a shared surface normal, there will be certain distances where the charge density templated by each cube align and reinforce (Figs. S8C,D). There will also be certain distances where the charge densities will be perfectly anti-aligned, leading to destructive interference of the charge density wave (Figs.S8E,F). Intuitively, destructive interference is energetically costly because planes of like charges interact without screening. As seen in Figs. S8E,F, the charge density at the midplane is near zero, indicating an equal mixture of charges, leading to a strong, repulsive interaction between the planes of like charge adjacent to the midplane. As will be discussed later, the high energy penalty for destructive interference leads to a unique phenomenology.

A decaying oscillatory interaction energy (Fig. S8A) will preclude nanocube flocculation since particles cannot assemble closer than a certain separation where the free energy maximum (peak) overpowers the thermal energy. However, such an energy profile also presents the possibility that nanocubes might become kinetically trapped (also known as reversible coagulation[28]) in local minima (e.g., point c in Fig. S8A). On the other hand, our simulations show that the colloidal stability can be increased by introducing slight tilting. In detail, we introduced frustration into the system by varying the nanocube surface normals. A relative tilt between nanocubes washes out the peaks and troughs of the interaction energy to some extent. Two nanocubes with a relative tilt can be thought of as a linear combination of many parallel plates at slightly different separations, since the effect of tilt is to introduce a range of separations between the plates (see Fig. S2A). So the energy of interaction of two tilted plates is just the average of the energies of many parallel plates at slightly different separations. A larger relative tilt introduces a larger range of separations over which the average must be taken, decreasing the oscillatory character of the interaction compared to that of the parallel case. Thus, a purely repulsive interaction without much oscillatory character can be observed (Fig. S8B). Note there is a significant difference in energy scales shown in Figs. S8A,B due to the diminishing oscillatory contribution. Allowing rotations of the nanocubes in simulations would lead to additional repulsive free energy beneficial for colloidal stability. This and other possibilities will be explored in future work.
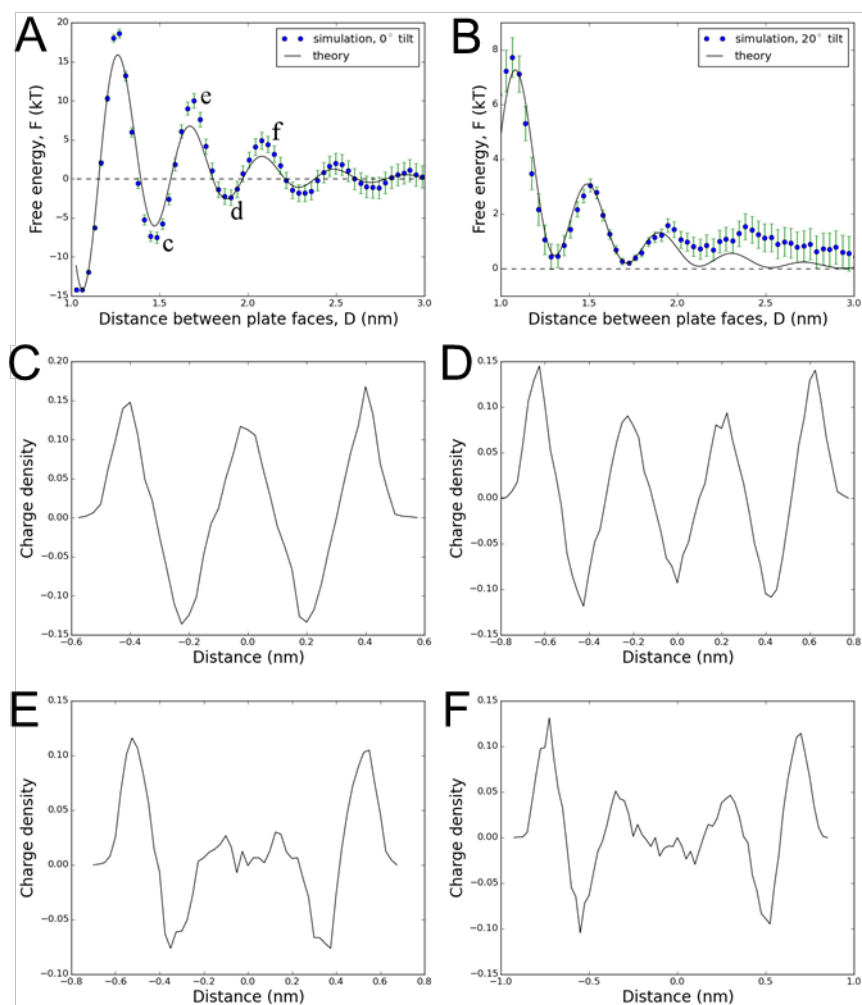
Fig. S8. Simulated free energies of layering (blue dots with error range) for two parallel (A) and tilted (B) nanocubes (2.45×1.85×1.85 nm³), and fit (solid lines) by the Ginzburg-Landau theory with Coulomb interactions (Eq. (13)). (C–F) Simulated charge densities between two parallel nanocubes located at troughs **(C,D)** and peaks **(E,F)** as marked in **(A)**; the Cd-bound Cl⁻ peaks have been omitted from the charge density profiles. Note that constructively interfering charge density profiles are low energy configurations and destructively interfering ones are high energy configurations.

Real NCs typically have spheroidal shape truncated with various low-index planes. Thus, we use a linear combination of differently tilted nanocubes as a first approximation to these spheroid NC facets in the spirit of the Derjaguin approximation. There are a few important points to address with regards to the approximation made here. In a real spheroidal NC, different facets have different surface compositions. In our simulations, we only consider Cd-terminated facets. As mentioned above,

interactions between [001] and [111] facets are equivalent to those between [001] and [001] facets (Fig. S6). Thus, we simplified the interactions between various Cd-terminated facets by replacing them with [001]-[001] interactions. In addition, we will be combining parallel nanocube and small tilt angle nanocube interactions only, which means we can treat these as interactions between flat plates, ignoring all nanocube faces except for the closest ones. Informed by the geometry of a faceted spheroidal zinc-blende CdSe NC, we show quasi-spheres formed from one parallel plate and four, six, or eight tilted plates (e.g., there are four [111]-like and four [011]-like facets for each [001]-like facet), as shown in Fig. S9. For CdSe NCs with a diameter of 10 nm (close to the upper limit of NC size used in our experiments), we find that the troughs are significantly reduced, while the peaks remain high compared to thermal energy (10–20 k_BT) as the two NCs begin to approach within around 1 nm between the closest facets. Such high energy peaks are estimated to be capable to provide long term colloidal stability. These simulation results support our experimentally observed colloidal stability of NCs with finite curvature in molten inorganic salts.
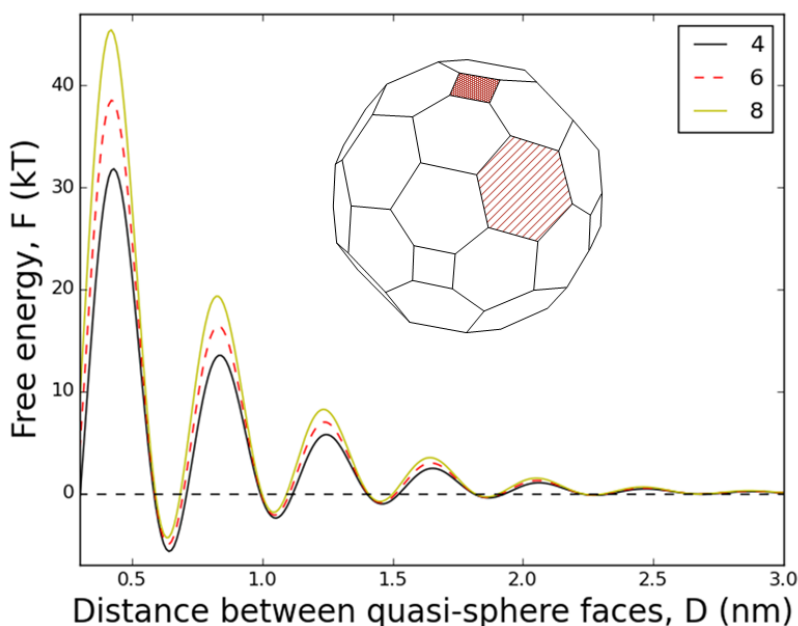

Fig. S9. **Simulated free energy of layering between two quasi-spherical CdSe NCs (10 nm in diameter) in molten KCl.** The quasi-spheres are formed by one parallel facet and 4, 6, or 8 tilted facets. Inset shows an example of quasi-spherical particle. The highlighted facets have four and six adjacent tilted facets contributing to the repulsive force between NCs.

In all the above simulations, we chose a temperature of 1250 K because it is well above the hysteresis loop for our molten salt model and still near the melting point of KCl (~1000 K). Note that

our molten salt model does not account for polarization fluctuations. However, we expect the above results such as the layering effect and the charge density profile should be general for a wide range of temperatures. In Fig. S10, we extract the density profiles near CdSe nanocubes at 1150 and 1200 K and measured the correlation lengths and peak heights. Our theory predicts that the amplitude of the energy of interaction should go as the square of the density at the NCs. Therefore these density profiles allow us to predict how to scale the free energy profiles for systems at these temperatures (Table S1).
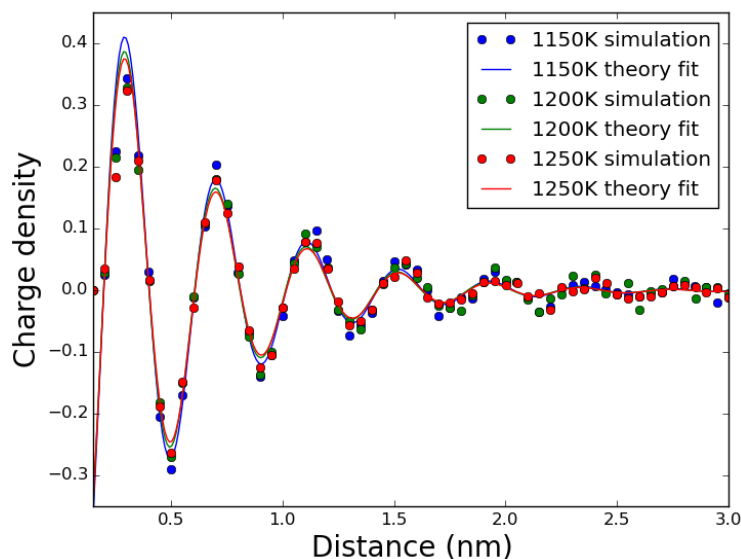

Fig. S10. Temperature dependence of charge ordering induced by CdSe nanocubes $(2.45 \times 1.85 \times 1.85$ nm$^3)$ **in molten KCl.** Note the first Cd-bound Cl$^-$ peak has been omitted from each charge density profile.

Table S1. Theory fits for CdSe nanocubes in molten KCl at various temperatures. F scaling indicates the appropriate factor to scale the interaction energy at 1250 K in order to find the interaction energy for a system at that temperature. The scaling is found simply by dividing the square of the amplitude, A at the desired temperature by the square of the amplitude at 1250 K.

T (K)	A (nm^{-3})	l_c (nm)	q_0 (nm^{-1})	φ	F scaling
1150	0.7454	0.496	15.3728	1.6758	1.139
1200	0.7161	0.4806	15.4125	1.6715	1.051
1250	0.6986	0.4783	15.3696	1.6673	1

l_c: Ginzburg-Landau correlation length; q_0: preferred wavenumber of layering; φ: phase shown in Eq. (4); F scaling: free energy per unit area

Simulations of ion layering on a structureless (or chemically inert) wall

For comparison, we also ran MD simulations on a system with structureless surfaces without chemical affinity to either ion in the molten KCl. The system has Lennard–Jones (L–J) interactions between the solvent and the structureless NC surfaces, and unmodified L–J and Coulomb interactions between the ions. We find that the ion density profiles templated by the structureless NC surfaces are similar to the density profiles of hard sphere templated by a hard wall. The interaction between the structureless NC surfaces is also very similar to the hard sphere-hard wall system. Without surface charge and/or different chemical affinity for different solvent, oscillatory ion layering observed earlier in the simulation study does not occur. Since much of solvation theory is based on the hard sphere-hard wall system and our control system behaves analogously to the hard sphere-hard wall system, we will briefly compare the phenomenology of the molten salt-NC system (with chemical affinity) and the hard sphere-hard wall system.

In the absence of surface charge or chemical affinity, ion layers still form, but not the alternating oscillations that occur in the presence of surface charge or chemical affinity. Near a hard wall, the density profile of a hard sphere fluid oscillates about the bulk density. The correlation length of these oscillations is related to the radius of the spheres. The solvent-mediated (hard sphere-mediated) interaction between two hard walls is oscillatory, but the source of the oscillations is related to the packing of the hard spheres between the walls (Fig. S11). The important factor for the hard sphere-hard wall interaction energy is the space available to the hard spheres to move, i.e., the entropy of the hard spheres. The peaks and troughs of this energy profile are based on the density of hard spheres at the midplane between the two hard walls. When the midplane density is less than the bulk density, the hard wall energy is near a trough; when the midplane density is above bulk, the energy is near a peak. Beyond this oscillating regime (<0.5 nm), the forces of interaction are usually attractive as demonstrated by our simulations and phenomenological theory (Fig. S11). These simulations on a structureless wall are in accordance with our experimental observations of destabilization of NCs in molten salts when there is no chemical affinity between NCs and the ions. We note that Ginzburg-Landau theory predicts repulsion between walls which each bind to a different component of the solvent, but we expect such interactions to be much weaker than the energy scales associated with frustration in inorganic molten salts.[37]

Returning to the NC in molten salt system, troughs and peaks correspond to, as discussed above, coherence and decoherence of the templated molten salt charge density. NC interaction energy is at a minimum when the charge density at the midplane is a peak or a trough. Peak energies occur when

there is suboptimal shielding between like-charged solvent layers, i.e., when the charge density at the midplane is zero. The dominant energy contribution determines how the energy depends on the density profiles, and in molten salts, the Coulomb interaction between templated solvent layers is by far the most dominant.
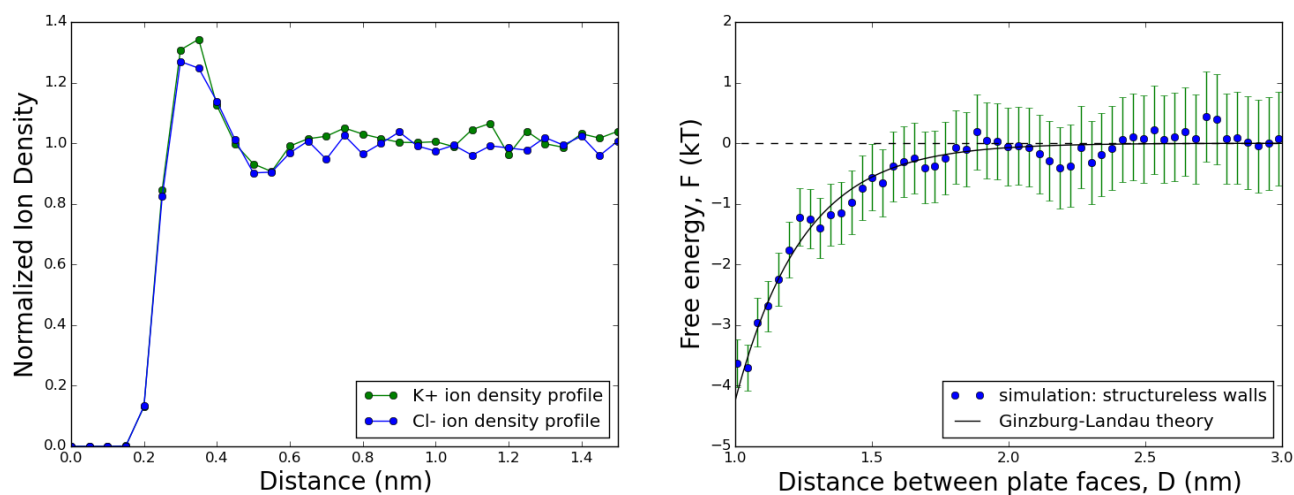

Fig. S11. Structureless walls are purely attractive. (Left) Density profiles of K^+ (green) and Cl^- (blue) around a hard wall. **(Right)** Simulated free energy between two structureless walls in molten KCl and the fit by Ginzburg-Landau theory. Structureless walls do not induce charge oscillations. As a result, the free energy is as predicted by the Ginzburg-Landau theory for solutes which perturb a field in a symmetric manner.

Details of Molecular dynamics (MD) simulation

We used the LAMMPS MD package[31] to simulate a molten salt-nanoparticle model system, specifically KCl salt with a CdSe NC. We adapted the models developed by Aguado et al. for molten salts[38] and by Grunwald et al. for solid CdSe[39]. These two models have different forms for the steric and dispersion interactions, with the molten salt using a Born-Mayer-Huggins form and the CdSe crystal using a 6–12 Lennard-Jones form[40]. We chose to use the Born-Mayer-Huggins potential, and adapted parameter values from Grunwald's force field by finding σ and ε for the Cd and Se ions. The parameters used for our model are displayed in Table S2. We simulated an NVT ensemble, with temperature at 1250 K (the melting point for our model is around 1000 K) and with KCl density of 20.681 nm^{-3}. We chose box sizes so that neighboring images of the CdSe nanocubes would have negligible interactions: the axis of allowed motion was 21.2 nm in length while the other two axes were 8.9 nm in length. Since the cubes were of size 2.45×1.85×1.85 nm^3 and the largest sampled separation

was ~3 nm, this box size leaves more than 16 nm between nearest nanocube images along the axis of motion. We used the LAMMPS-implemented particle-particle particle-mesh solver to implement the long-range Coulomb interactions. We implemented enhanced sampling using the PLUMED code plugin[34]. As a control, we simulated a structureless wall, with no charge and which interacted with solvent only through the 6–8 Lennard-Jones potential. The structureless walls displayed a standard solvent density profile. But long range charge-density oscillations were not observed as there was no surface charge to prefer one ion over the other. Two structureless walls assembled as predicted by the Ginzburg-Landau theory for solutes with a symmetric effect on the order parameter.

Table S2. MD model parameterization

$$E_{disp} = A \exp(-r/\rho) - \frac{C}{r^6} + \frac{D}{r^8}$$

Parameterization of CdSe NCs at 1250 K

	A (k_BT)	ρ (Å)	D (k_BT Å^8)	C (k_BT Å^6)	ε (k_BT)	σ (Å)
K–K	13763	0.339	−139	141	146	0.994
Cl–Cl	18019	0.337	−1448	721	89	1.417
K–Cl	14579	0.342	−423	278		
Cd–K	14087	0.2	66	30		
Se–K	14087	0.5	23284	2391		
Cd–Cl	14087	0.1	152	151		
Se–Cl	14087	0.5	31158	2810		

Parameterization of structureless wall at 1250 K

	A (k_BT)	ρ (Å)	D (k_BT Å^8)	C (k_BT Å^6)	ε (k_BT)	σ (Å)
K–K	13763	0.339	−139	141	146	0.994
Cl–Cl	18019	0.337	−1448	721	89	1.417
K–Cl	14579	0.342	−423	278		
Wall–K	0	0	14087	1409		
Wall–Cl	0	0	14087	1409		

III. Derjaguin-Landau-Verwey-Overbeek (DLVO) calculations and screening length

Here we describe how the double layer repulsion, U_{dl}, and the van der Waals attraction, U_{vdW}, as presented in Fig. S3C and Fig. 3f in the main text were estimated for the CdSe NCs in molten KCl.

The non-retarded van der Waals interaction between two flat surfaces interacting across the solvent medium separated by a distance D is given (per unit area) by

$$u^{fl}_{vdW}(D) = -\frac{A}{12\pi}\frac{1}{D^2}\ ,\tag{14a}$$

and between two spherical particles of radius R separated by a distance D at the point of closest approach:

$$U^{sp}_{vdW}(D) = -\frac{A}{6}\left[\frac{2R^2}{(4R+D)D}+\frac{2R^2}{(2R+D)^2}+\ln\frac{(4R+D)D}{(2R+D)^2}\right],\tag{14b}$$

where A is the Hamaker constant, a material parameter whose value is specific to the nanocrystal-solvent system[11]. Typically, this is estimated from the Lifshitz theory and optical absorption spectra of the material.

A commonly used convenient approximate expression for the Hamaker constant (valid when retardation effects are absent, i.e., small D) and the spectrum is characterized by one dominant absorption peak[11],

$$A \simeq \frac{3}{4}k_BT\left(\frac{\epsilon_p-\epsilon_s}{\epsilon_p+\epsilon_s}\right)^2 + 3h\frac{v_e}{16\sqrt{2}}\frac{(n_p^2-n_s^2)^2}{\left(n_p^2+n_s^2\right)^{\frac{3}{2}}}\ ,\tag{15}$$

where ε_P and ε_S are the relative dielectric constants of particles and solvent media, n_P and n_S are the refractive indices of particles and solvent media, h is the Planck constant (6.63×10^{-34} J s), and v_e is the frequency of the main electronic absorption of the dielectric perimittivity, taken as 3×10^{15} Hz for ILs. The static contribution to the Hamaker constant, i.e., the first term in Eq.(15), is very small as conducting media like molten inorganic salts largely screen out the static dipole contributions. The Hamaker constant evaluated with the typical values for electronic absorption frequency and refractive indices, is $A\sim 5\times10^{-20}$ J.

We now show that the Hamaker constant can be obtained for the specific case of CdSe interactions KCl from values known in the literature, and show that the above approximation results in a value that is reasonably accurate. For this we use a combination formula for the Hamaker constants, $A_{121}\sim\left(\sqrt{A_{11}}-\sqrt{A_{22}}\right)^2$, where A_{ii} indicates interaction of two particles of type i across vacuum, and A_{iji} indicates interactions of two particles of type i interacting across the medium of material j. Using values for Hamaker constant for CdSe interacting in vacuum[41,42], $A_{11} = 11\times10^{-20}$ J, and KCl interacting in vacuum[42], $A_{22} = 6.2\times10^{-20}$ J, and using the combination formula, we arrive at the relevant Hamaker

constant for CdSe particles interacting in KCl medium, $A_{121} = 7\times10^{-21}$ J, which is an order of magnitude lower than that estimated from Eq. (15) for generic dielectric. However, the value used here is for crystalline KCl and we expect A_{22} to be somewhat lower in molten KCl. The value of Hamaker constant in practice should not be so different from $A \sim 5\times10^{-20}$ J estimated above for generic solutes in molten salts.

The electric double layer forces are estimated within the context of the mean-field Poisson-Boltzmann theory where the Debye screening length, l_s, depends on the number density of the salt ions, n_s, as $l_s^{-2} = n_s \frac{e^2}{\epsilon_0 \epsilon k_B T} = n_s l_B$, where $l_B \equiv \frac{e^2}{(\epsilon \epsilon_0 k_B T)}$ is the Bjerrum length. The density of ions for molten salt at this temperature (n_s, 20.7 nm^{-3}) suggests a very small Debye length (0.06 nm), assuming a relative permittivity (ε) of 4. This suggests that double layer forces are effectively screened out and insignificant. The free energy of double layer interactions can be expressed in terms of the surface potential (measured to be $v_s = 50 \, mV$ for the CdSe NC used in the experiments) as[11]:

$$U_{dl}(D) = 2 \, \epsilon \, \epsilon_0 v_s^2 l_s^{-1} e^{-\frac{D}{l_c}} \tag{16}$$

As a word of caution, the Debye-Hückel approximation is strictly valid only for dilute electrolytes and does not account for finite size and correlation effects of the ions that are more important in concentrated electrolytes. These effects may be explained within a more general theoretical framework[22] that should also predict long-range charge density layering in concentrated electrolytes consistent with our phenomenological theory and simulations. To account for the possibility of long-range double layer repulsion due to interionic correlations, we measured the screening length from the atomistic simulations by extracting the bulk charge-charge correlation function[43]. The effective screening length in our simulated molten salt at a temperature of 1250 K and 1 bar pressure was found to be 0.63 nm (Fig. S12), which is about an order of magnitude larger than the Debye length estimated from the Debye-Hückel approximation. This estimate is in agreement with results from previous simulations[43] and suggests that our calculations are in a regime where the importance of ionic correlations is high. Recent experiments on concentrated aqueous electrolytes[21] and room temperature organic ionic liquids[20] also indicate significantly longer effective screening lengths than those predicted within the Debye-Hückel approximation. Large effective screening length is expected to further improve the colloidal stability of particulates in molten inorganic salts. We anticipate that it will be possible to extend our phenomenological theory to explain such effects by including higher order ionic correlations[22,44]. This work is in progress.
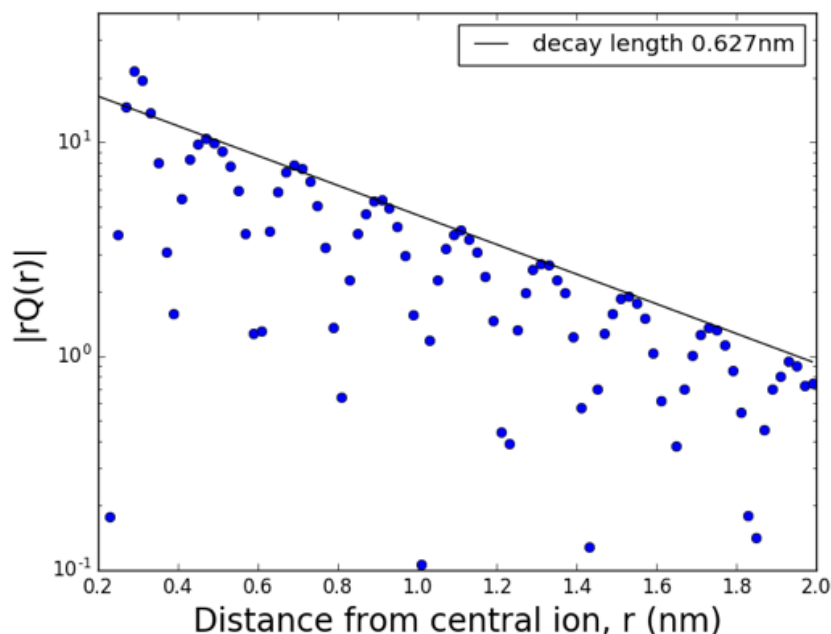
Fig. S12. Charge-charge correlations in a simulated molten salt. The screening length is identified as the exponential decay length of the oscillating charge-charge correlations[43]. The screening length is 0.627 nm at 1250 K temperature and the pressure 1 bar.

IV. Characterization of nanocrystal dispersions in organic ionic liquids (ILs)

CdSe NCs recovered from P^+P^- IL show vibration peaks similar to those of NCs with original ligands (OA/TOP/TOPO) rather than P^+P^-, indicating the preservation of the NC ligand shell when dispersed in P^+P^- **(Fig. S13A and B)**. On the contrary, the FTIR features of NCs recovered from $[BMIM]^+Cl^-$ resembled those of pure $[BMIM]^+Cl^-$, which suggests the replacement/removal of original organic ligands by $[BMIM]^+Cl^-$ solvent molecules. The assignment of resonances to different protons in free OA and OA bound on CdSe NCs[45] is shown in **Fig. S13C and D**. The resonances of protons in TOP and TOPO ligands are within the range of 1.0 to 1.8 ppm and mostly overlap with those of the methylene and methyl ($-CH_2-$ and $-CH_3$) groups in OA. The characteristic resonance for alkene protons (position 5) in free OA is at 5.45 ppm **(C)**; this broadens and shifts to a lower field (5.57 ppm) when bound on CdSe NC surfaces **(Fig. S13D)**[45]. This resonance is also observed in CdSe NCs in P^+P^- diluted with d^8-toluene (P^+P^-/d^8-toluene = 1:10 v/v) (inset in **(Fig. S13F)**). The amount of OA ligands in CdSe NC colloids (calibrated by the concentration of CdSe NCs) remains almost unchanged when

dispersed in toluene or P$^+$P$^-$, as shown in **(Fig S13H)**. To check the existence of OA ligands in CdSe NCs in [BMIM]$^+$Cl$^-$, the IL matrix was dissolved with DI water. The insoluble CdSe NCs were digested by half-concentrated aqua regia and then the OA ligands, if any, were extracting using diethyl ether. This solution was dried under vacuum, and then diluted in d^8-toluene for NMR measurements. No resonances from OA ligands were observed **(Fig.S13G)**, indicating the complete removal of native ligands during the phase transfer of CdSe NCs from octane to [BMIM]$^+$Cl$^-$.
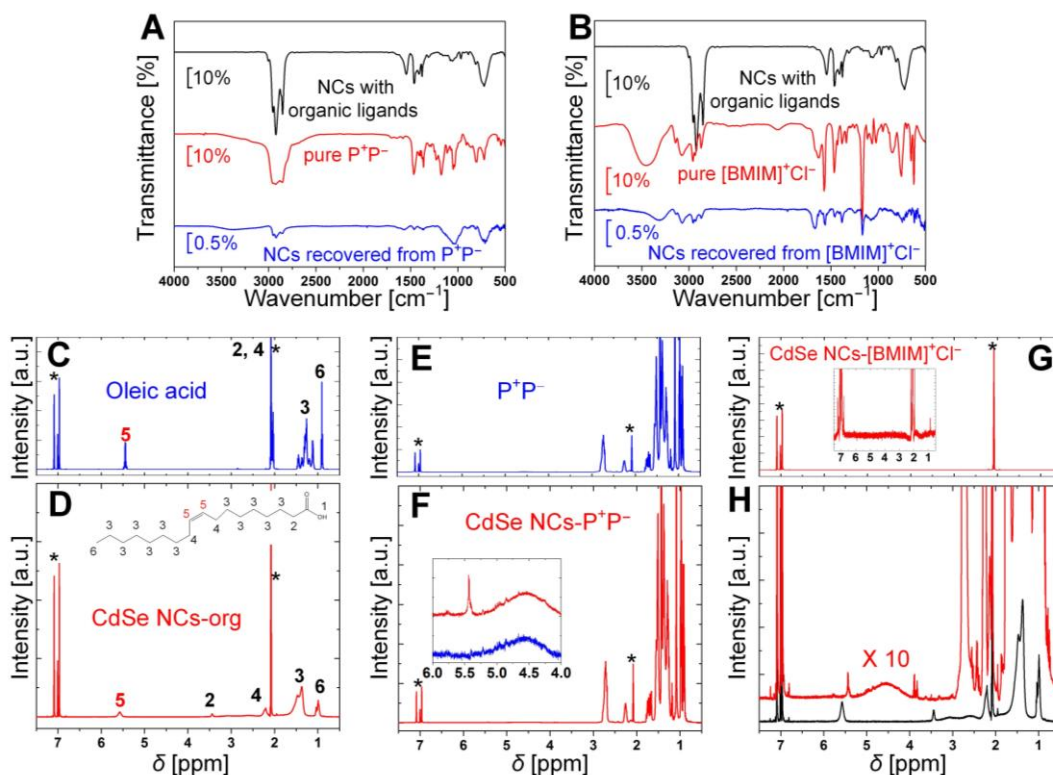

Fig. S13. Surface chemistry of nanocrystals in ionic liquids. FTIR spectra of CdSe NCs with organic ligands (OA/TOP/TOPO) and recovered from their stable colloids in **(A)** P$^+$P$^-$ and **(B)** [BMIM]$^+$Cl$^-$. In both cases, the spectra of pure ILs (red curves) are shown for reference. Intensities of recovered NC spectra are magnified 20 times. ^{1}H-NMR of **(C)** OA in d^8-toluene and **(D)** CdSe NCs with original organic ligands (OA/TOP/TOPO) in d^8-toluene (25 mg/mL, 1.0 mL). The assignment of resonances to different protons in OA and OA on the CdSe NC surface is indicated in the inset in **(D)**. **(E)** P$^+$P$^-$ in d^8-toluene, **(F)** CdSe NCs in P$^+$P$^-$ diluted by d^8-toluene (2.5 mg/mL, 1.0 mL, P$^+$P$^-$/d^8-toluene = 1:10 v/v). Inset in **(F)** compares the OA alkene protons resonances of CdSe NCs in P$^+$P$^-$ (red curve, overshadowed by the strong resonances from P$^+$P$^-$ solvent in D) versus pure P$^+$P$^-$ (blue curve). **(G)** Residue recovered from digested CdSe NCs in [BMIM]$^+$Cl$^-$. No OA resonance is present (inset in **(G)**). **(H)** Comparison of ^{1}H NMR of CdSe NCs with organic ligands in d^8-toluene (black curve) and in P$^+$P$^-$/d^8-toluene (1:10 v/v) (red curve). (*) indicates the residual solvent resonances in **(C–H)**.

ICP–OES analysis suggests almost no change in the amount of the P-containing surfactants (TOP and TOPO) for CdSe NCs in toluene (Cd:Se = 1.2, P:Se = 0.037 in moles) and recovered from P$^+$P$^-$ (Cd:Se = 1.1, P:Se = 0.030 in moles). In contrast, TOP and TOPO ligands were replaced/removed during the phase transfer of CdSe NCs from octane to the Lewis basic [BMIM]$^+$Cl$^-$ (no P detected). Thus, CdSe NCs are stabilized in [BMIM]$^+$Cl$^-$ purely by solvent molecules.

The above analysis depicts the fate of native organic ligands on CdSe NCs in different types of ILs. The organic ligands of CdSe NCs remained in the hydrophobic P$^+$P$^-$, but were completely removed and replaced before being transferred in [BMIM]$^+$Cl$^-$ or [BMIM]$^+$I$^-$. In another experiment, naked CdSe or QDs NCs did not disperse well in P$^+$P$^-$, emphasizing the importance of native organic ligands in the stabilization of NCs in P$^+$P$^-$. However, we cannot rule out the possibility that the anionic part of P$^+$P$^-$ (bis(2,4,4-trimethylpentyl)phosphinate) may also behave like additional NC ligands due to its nucleophilicity[46]. In addition, the equilibrium of free and bound OA ligands on CdSe NCs may change in P$^+$P$^-$.

Supplementary References

S1   Igarashi, K. *et al.* Properties of KSCN-rich molten NaSCN-KSCN mixtures. *Z. Naturforsh.* **46a**, 540–544 (1991).

S2   Dancy, E. A. & Nguyen-Duy, P. Calorimetric determination of the thermodynamic properties of the binary eutectics in the NaNO$_3$–Ca(NO$_3$)$_2$ and KNO$_3$–Ca(NO$_3$)$_2$ systems. *Thermochimica Acta* **42**, 59–63 (1980).

S3   Janz, G. J. & Truong, G. N. Melting and premelting properties of the KNO$_3$–NaNO$_2$–NaNO$_3$ eutectic system. *J. Chem. Eng. Data* **28**, 201–202 (1983).

S4   Cordaro, J. G., Kruizenga, A. M., Altmaier, R., Sampson, M. & Nissen, A. in *SolarPACES* (Granada, Spain, 2011).

S5   Wang, C., Daimon, H., Onodera, T., Koda, T. & Sun, S. A general approach to the size- and shape-controlled synthesis of platinum nanoparticles and their catalytic reduction of oxygen. *Angew. Chem. Int. Ed.* **47**, 3588–3591 (2008).

S6   Dirin, D. N. *et al.* Lead halide perovskites and other metal halide complexes as inorganic capping ligands for colloidal nanocrystals. *J. Am. Soc. Chem.* **136**, 6550–6553 (2014).

S7   Son, J. S., Lee, J.-S., Shevchenko, E. V. & Talapin, D. V. Magnet-in-the-semiconductor nanomaterials: High electron mobility in all-inorganic arrays of FePt/CdSe and FePt/CdS core–shell Heterostructures. *J. Phys. Chem. Lett.* **4**, 1918–1923 (2013).

S8   Park, J. *et al.* Ultra-large-scale syntheses of monodisperse nanocrystals. *Nat. Mater.* **3**, 891–895 (2004).

S9   Baek, J., Allen, P. M., Bawendi, M. G. & Jensen, K. F. Investigation of indium phosphide

nanocrystal synthesis using a high-temperature and high-pressure continuous flow microreactor. *Angew. Chem. Int. Ed.* **50**, 627–630 (2011).

S10   Battaglia, D. & Peng, X. Formation of high quality InP and InAs nanocrystals in a noncoordinating solvent. *Nano Lett.* **2**, 1027–1030 (2002).

S11   Zhang, H., Jang, J., Liu, W. & Talapin, D. V. Colloidal nanocrystals with inorganic halide, pseudohalide, and halometallate ligands. *ACS Nano* **8**, 7359–7369 (2014).

S12   Punjabi, A. *et al.* Amplifying the red-emission of upconverting nanoparticles for biocompatible clinically used prodrug-induced photodynamic therapy. *ACS Nano* **8**, 10621–10630 (2014).

S13   Hansen, J.-P. & McDonald, I. R. *Theory of Simple Liquids. 4th Ed.*, (Elsevier Academic Press, 2013).

S14   Bazant, M. Z., Storey, B. D. & Kornyshev, A. A. Double layer in ionic liquids: Overscreening versus crowding. *Phys. Rev. Lett.* **106**, 046102 (2011).

S15   Limmer, D. T. Interfacial ordering and accompanying divergent capacitance at ionic liquid-metal interfaces. *Phys. Rev. Lett.* **115**, 256102 (2015).

S16   Derjagin, B. V. & Landau, L. Theory of the stability of strongly charged lyophobic sols and of the adhesion of strongly charged particles in solution of electrolytes. *Acta Physicochimica USSR* **14**, 633–662 (1941).

S17   Hertlein, C., Helden, L., Gambassi, A., Dietrich, S. & Bechinger, C. Direct measurement of critical casmir forces. *Nature* **451**, 172–175 (2008).

S18   Di Cicco, A. *et al.* Short-range order in solid and liquid KBr probed by EXAFS. *J. Phys.: Condens. Matter.* **8**, 10779– 10797 (1996).

S19   Heyes, D. M. & Clarke, J. H. R. Computer simulation of molten-salt interphases. Effect of a rigid boundary and an applied electric field. *J. Chem. Soc., Faraday Trans. 2* **77**, 1089–1100 (1981).

S20   Gebbie, M. A., Dobbs, H. A., Valtiner, M. & Israelachvili, J. N. Long-range electrostatic screening in ionic liquids. *Proc. Natl. Acad. Sci. U.S.A.* **112**, 7432–7437 (2015).

S21   Smith, A. M., Lee, A. A. & Perkin, S. The electrostatic screening length in concentrated electrolytes increases with concentration. *J. Phys. Chem. Lett.* **7**, 2157–2163 (2016).

S22   Lee, B. P. & Fisher, M. E. Charge oscillations in Debye-Hückel theory. *Europhys. Lett.* **39**, 611–616 (1997).

S23   Low, U., Emery, V. J., Fabricius, K. & Kivelson, S. A. Study of an Ising model with competing long- and short-range interactions. *Phys. Rev. Lett.* **72**, 1918 (1994).

S24   Fredrickson, G. H. Surface ordering phenomena in block copolymer melts. *Macromolecules* **20**, 2535–2542 (1987).

S25   Gavish, N. & Yochelis, A. Theory of phase separation and polarization for pure ionic liquids. *J. Phys. Chem. Lett.* **7**, 1121–1126 (2016).

S26   Seul, M. & Andelman, D. Domain shapes and patterns: The phenomenology of modulated phases. *Science* **267**, 476–483 (1995).

S27   Mezger, M. *et al.* Molecular layering of fluorinated ionic liquids at a charged sapphire (0001) surface. *Science* **322**, 424–428 (2008).

S28   Israelachvili, J. N. *Intermolecular and surface forces, third ed.*, 1–674 (Elsevier Academic Press, 2011).

S29   Chaikin, P. M. & Lubensky, T. C. *Principles of Condensed Matter Physics*. (Cambridge Univ. Press, 2000).

S30   Tsori, Y., Andelman, D. & Schnick, M. Defects in lamellar diblock copolymers: Chevron- and Ω-shaped tilt boundaries. *Phys. Rev. E* **61**, 2848 (2000).

S31   Plimpton, S. Fast parallel algorithms for short-range molecular dynamics. *J. Comput. Phys.* **117**, 1–19 (1995).

S32   Pensado, A. S. & Padua, A. A. H. Solvation and stabilization of metallic nanoparticles in ionic

liquids. *Angew. Chem. Int. Ed.* **50**, 8683–8687 (2011).

S33   Zobel, M., Neder, R. B. & Kimber, S. A. J. Universal solvent restructuring induced by colloidal nanoparticles. *Science* **347**, 292–294 (2015).

S34   Tribello, G. A., Bonomi, M., Branduarda, D., Camilloni, C. & Bussi, G. PLUMED 2: New feathers for an old bird. *Comput. Phys. Commun.* **185**, 604–613 (2014).

S35   Shirts, M. R. & Chodera, J. D. Statistically optimal analysis of samples from multiple equilibrium states. *J. Chem. Phys.* **129**, 124105 (2008).

S36   Frenkel, D. & Smit, B. *Understanding molecular simulation, second ed.*, 165–199 (Elsevier Academic Press, 2002).

S37   Marcelja, S. & Radic, N. Repulsion due to boundary water. *Chem. Phys. Lett.* **42**, 129–130 (1976).

S38   Aguado, A. & Madden, P. A. Molecular dynamics simulations of the liquid-vapor interface of a molten salt. III. Size asymmetry effects and binary mixtures. *J. Chem. Phys.* **117**, 7659–7668 (2002).

S39   Grünwald, M., Zayak, A., Neaton, J. B., Geissler, P. L. & Rabani, E. Transferable pair potentials for CdS and ZnS crystals. *J. Chem. Phys.* **136**, 234111 (2012).

S40   Fumi, F. G. & Tosi, M. P. Ionic sizes and Born repulsive parameters in the NaCl-type alkali halides–I: The Huggins-Mayer and Pauling forms. *J. Phys. Chem. Solids* **25**, 31–43 (1964).

S41   Jana, S. *et al.* Stacking and colloidal stability of CdSe nanoplatelets. *Langmuir* **31**, 10532−10539 (2015).

S42   Bergström, L. Hamaker constants of inorganic materials. *Adv. in Colloid Interface Sci.* **70**, 125−169 (1997).

S43   Keblinski, P., Eggebrecht, J., Wolf, D. & Phillpot, S. R. Molecular dynamics study of screening in ionic fluids. *J. Chem. Phys.* **113**, 282−291 (2000).

S44   Leote de Carvalho, R. J. F. & Evans, R. The decay of correlations in ionic fluids. *Molecular Physics* **83**, 619−654 (1994).

S45   Fritzinger, B., Capek, R. K., Lambert, K., Martins, J. C. & Hens, Z. Utilizing self-exchange to address the binding of carboxylic acid ligands to CdSe quantum dots. *J. Am. Chem. Soc.* **132**, 10195–10201 (2010).

S46   Green, M., Rahman, P. & Smyth-Boyle, D. Ionic liquid passivated CdSe nanocrystals. *Chem. Commun.*, 574–576 (2007).